Journal of Ultrafine Grained and Nanostructured Materials
https://jufgnsm.ut.ac.ir
Vol. 51, No.1, June 2018, pp. 26-31
Print ISSN: 2423-6845 Online ISSN: 2423-6837
DOI: 10.22059/JUFGNSM.2018.01.04

Effect of fuel content on structural and magnetic properties of solution combusted $Mn_{0.8}Zn_{0.2}Fe_2O_4$ powders

Mohammad Naserifar, Seyyed Morteza Masoudpanah*, Somaye Alamolhoda

School of Metallurgy & Materials Engineering, Iran University of Science and Technology (IUST), Narmak, Tehran, Iran .

Recieved: 29 December 2017; Accepted: 17 February 2018

** Corresponding author email: masoodpanah@iust.ac.ir*

ABSTRACT

Single phase $Mn_{0.8}Zn_{0.2}Fe_2O_4$ powders were synthesized by solution combustion method. The solution combustion method relies on the exothermic self-sustained reactions in reactive solution containing of oxidizers and organic fuels. In this work, the effects of various amounts of glycine as fuel on the powder characteristics were investigated. The structure, cation distribution, microstructure and magnetic properties were characterized by X-ray diffraction, electron microscopy and vibrating sample magnetometry techniques. The cation distributions determined by Bertaut method in which the observed reflection intensities compared with the calculated ones for supposed crystal structures. The $Mn_{0.8}Zn_{0.2}Fe_2O_4$ exhibited partially inverse structure in which Zn preferentially occupied tetrahedral (A) sites. The as-combusted $Mn_{0.8}Zn_{0.2}Fe_2O_4$ powders showed spongy structure due to the liberation a large amount of gaseous products. However, the porosity decrease with the increase of fuel content due to the increase of adiabatic combustion temperature. The saturation magnetization of the as-combusted $Mn_{0.8}Zn_{0.2}Fe_2O_4$ powders increased from 43 to 69 emu/g with the increase of f from 0.5 to 1 and then slightly decreases to 67 emu/g for ϕ=1.5. The highest saturation magnetization (69 emu/g) for ϕ=1 was attributed to the highest crystallite size and crystallinity. The coercivity also increased from 27 to 67 Oe with fuel content.

Keywords: *$Mn_{0.8}Zn_{0.2}Fe_2O_4$; Solution combustion synthesis; Fuel; Magnetic properties.*

1. Introduction

Spinel magnetic ferrite nanoparticles have been found many applications in magnetic fluids, drug delivery, microwave devices, sensors, catalysis, etc., due to their unique physical properties and excellent chemical stability [1, 2]. The spinel ferrites have cubic structure of 32 closely packed oxygen atoms with 64 tetrahedral sites and 32 octahedral sites from which only 8 tetrahedral (A) and 16 octahedral [B] sites are occupied for electrical neutrality [3]. Among the spinel ferrites, MnZn ferrites ($Mn_{1-x}Zn_xFe_2O_4$) have attracted much attention for their high saturation magnetization, high electrical resistivity and low power loss [4, 5]. However, the various structural, electrical and magnetic properties of spinel ferrites strongly depend on phase, cation distribution, size and morphology of particles, etc. via composition, nature of substituent(s) and preparation methods [6].

MnZn ferrite nanoparticles have been synthesized by various synthesis methods such as ball milling [7], coprecipitation [8], solvothermal [9], sol–gel [10] and solution combustion synthesis (SCS) [11]. Among these methods, SCS is a simple, energy- and time-efficient method

for mass production of nanomaterials [12]. SCS relies on the exothermic self-sustained reactions in reactive solution including of oxidizers such as nitrates, sulfates and carbonates and organic fuels such as urea, glycine, citric acid, sucrose, etc. [13]. The released thermal energy by combustion reaction along with molecular level mixing is enough for direct synthesis of well crystalline multicomponent complicated structures as spinels, garnets, perovskites, superconductors, etc. [12, 14, 15]. Furthermore, a rapid decrease of temperature after combustion reaction by exhausting of gaseous products results in the porous nanostructures [10, 16]. The fuel nature and content mainly control the as-combusted powder characteristics such as phase, morphology, particle size and surface area [17]. The organic fuels are source of carbon and hydrogen for burning and can form complexes with metal cations, thus facilitating homogeneous mixing of cations in solutions or gels [18]. The urea, glycine, citric acid and glucose are the most commonly used fuels in combustion reactions, due to their high solubility in water, low decomposition temperature (below 400 °C), compatibility with metal nitrates and availablity [19]. Lazarova et al. [17] showed the NH_2-contained fuels (e. g. urea and glycine) lead to the as-combusted powders with the larger particle size and higher aggregation ability in comparison with pure carbohydrate fuels (e. g. glucose and sucrose). Shafiu et al. [20] investigated the magnetic properties of $MnFe_2O_4$-PVA nanocomposites prepared by solution combustion method using ethylene glycol as fuel. Yu and Yang also synthesized $MnFe_2O_4$ powders with the saturation magnetization of 50.1 emu/g and coercivity of 56.1 Oe by using citric acid fuel [21].

In this work, the effects of fuel to oxidant ratios (φ=0.5, 1 and 1.5) on the structure, cation distribution, microstructure and magnetic properties of MnZn ferrite powders were investigated. Single phase $Mn_{0.8}Zn_{0.2}Fe_2O_4$ powders were directly synthesized by solution combustion using glycine as fuel at all φ values. However, the highest saturation magnetization of 69 emu/g was achieved for φ=1 on account of its highest particle size and highest crystallinity.

2. Experimental procedure

The required amounts of glycine ($C_2H_5NO_2$), ferric nitrate ($Fe(NO_3)_3.9H_2O$), manganese nitrate ($Mn(NO_3)_2.4H_2O$) and zinc nitrate ($Zn(NO_3)_2.6H_2O$) obtained from Merck Co. were dissolved in the distilled water in which the different fuel to oxidant molar ratios (φ) of 0.5, 1 and 1.5 were used without adjusting of pH. The dark brown homogeneous solution was poured into a dish and heated till to transform into a gel while by further heating up to 250 °C, ignition reaction started from a point and propagated spontaneously towards the walls of the dish. The combusted powders were hand-crushed with a pestle.

Phase evolution was analyzed by PANalytical X-ray diffractometer (XRD) using monochromatic CuKα radiation. The average crystallite size was also calculated from the width (311) peak using Scherrer's equation. The cation distributions were calculated by analysis of XRD patterns using Bertaut method.

The morphology and microstructure of the powders were observed by TESCAN Vega II field emission scanning electron microscopy.

A vibrating sample magnetometer (Meghnatis Daghigh Kavir Co., Iran) was also employed to measure the magnetic properties of the powders at room temperature.

3. Results and discussion

It is known that the fuel nature and fuel to oxidant ratio effect on the combustion behavior, phase constituents, morphology and electrical and magnetic properties of the as-combusted products [12, 22, 23]. Considering the typical combustion reaction byproducts as CO_2, N_2 and H_2O, the redox processes that are taking place during combustion reactions using glycine fuel can be written according to eq. 1:

$$0.8Mn(NO_3)_2 + 0.2Zn(NO_3)_2 + 2Fe(NO_3)_3 + \frac{40\varphi}{9}C_2H_5NO_2 + 10(\varphi-1)O_2 \rightarrow Mn_{0.8}Zn_{0.2}Fe_2O_4 + \frac{80\varphi}{9}CO_2 + \frac{100\varphi}{9}H_2O + (4+\frac{20\varphi}{9})N_2 \quad \text{(eq. 1)}$$

The maximum temperature reached during combustion under no energy loss condition, known as adiabatic combustion temperature, is maximum for stoichiometric mixture (φ=1) and decreased for $\phi \neq 1$, due to the need to heat up the excess reactants or products [19].

Fig. 1 shows the XRD patterns of the as-combusted $Mn_{0.8}Zn_{0.2}Fe_2O_4$ powders at the different φ values. The indexed peaks as (220), (311), (222), (400), (422), (511) and (440) related to cubic spinel structure (JCPDS card no. 74-2402) show the as-combusted powders are single phase MnZn

ferrite. Without need of further heat treatment, the MnZn ferrites are directly formed following solution combustion. Table 1 compares the cation distribution, lattice parameter and crystallite size of $Mn_{0.8}Zn_{0.2}Fe_2O_4$ powders. The cation distribution can be obtained from the analysis of XRD patterns by Bertaut method in which the observed intensity ratios $\left(\frac{I_{hkl}}{I_{\acute{h}\acute{k}\acute{l}}}\right)_{Obs.}$ were compared with the calculated intensity ratios $\left(\frac{I_{hkl}}{I_{\acute{h}\acute{k}\acute{l}}}\right)_{Calc.}$ [24]. The relative integrated intensity of a given diffraction line from powder specimens can be calculated by the following formula:

$$I_{hkl} = |F_{hkl}|^2 P L_p \quad \text{(eq. 2)}$$

which P is the multiplicity factor, Lp is the Lorentz-polarization factor which depends only on Bragg's diffraction angle θ, described as follows [25]:

$$L_p = \frac{1+cos^2 2\theta}{sin^2\theta cos2\theta} \quad \text{(eq. 3)}$$

and F_{hkl} is the structure factor which can be described for 220, 400 and 422 planes as follows [26]:

$$F_{220} = -8F_A + 16f_O(cos8\pi u - 1) \quad \text{(eq. 4)}$$

$$F_{400} = 8(F_A - F_B + 4f_O cos8\pi u) \quad \text{(eq. 5)}$$

$$F_{422} = -8F_A + 8f_O(cos16\pi u - 2cos8\pi u + 1) \quad \text{(eq. 6)}$$

which u is oxygen positional parameter, f_O is scattering factor of oxygen atom and F_A and F_B are the total scattering factor of atoms in A- and B-sites, respectively. For $(Zn_{0.20}Mn_{1-\delta}Fe_{\delta})_A[Mn_{\delta}Fe_{2-d}]_BO_4$, F_A

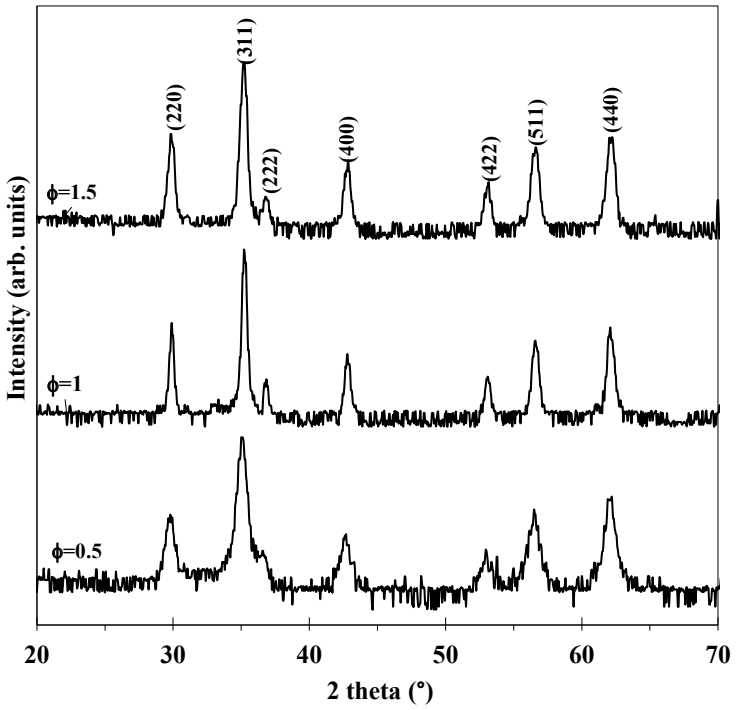

Fig. 1- XRD patterns of the as-combusted $Mn_{0.8}Zn_{0.2}Fe_2O_4$ powders at the various ϕ values.

Table 1- The cation distribution, lattice parameter and crystallite size of $Mn_{0.8}Zn_{0.2}Fe_2O_4$ as a function of ϕ values

ϕ	Cation distribution	$a_{exp.}$ (Å)	$a_{th.}$ (Å)	Crystallite size (nm)
0.5	$(Mn_{0.19}Zn_{0.20}Fe_{0.61})_A[Mn_{0.61}Fe_{1.39}]_BO_4$	8.2457	8.2466	10
1	$(Mn_{0.12}Zn_{0.20}Fe_{0.68})_A[Mn_{0.68}Fe_{1.32}]_BO_4$	8.2425	8.2439	37
1.5	$(Mn_{0.13}Zn_{0.20}Fe_{0.67})_A[Mn_{0.67}Fe_{1.33}]_BO_4$	8.2436	8.2443	25

and F_B can be written as

$$F_A = 0.2f_{Zn} + (1-\delta)f_{Mn} + \delta f_{Fe} \quad \text{(eq. 7)}$$

$$F_B = \delta f_{Mn} + (2-\delta)f_{Fe} \quad \text{(eq. 8)}$$

which f_{Zn}, f_{Fe} and f_{Mn} are scattering factors of zinc, iron and manganese atoms, respectively. The peaks' intensity ratios like I_{220}/I_{400}, I_{220}/I_{422} and I_{422}/I_{400} as a function of δ calculated and compared with the observed ratios for exploring the minimum of agreement factor (R) [27]:

$$R = \left(\frac{I_{hkl}}{I_{\acute{h}\acute{k}\acute{l}}}\right)_{Obs.} - \left(\frac{I_{hkl}}{I_{\acute{h}\acute{k}\acute{l}}}\right)_{Calc.} \quad \text{(eq. 9)}$$

It should be noted that there is no need for the thermal correction because of the spinel's high melting point and hence very small thermo-vibration effect of spinel on XRD patterns. The cation site occupancy mainly depends on the ionic radius, crystal field, electronic configuration and ionic polarization of M^{2+} cations [27]. Cation distributions show that the $Mn_{0.8}Zn_{0.2}Fe_2O_4$ powders have a partially inverse structure in which the divalent cations (Mn^{2+}) are distributed in tetrahedral (A) and octahedral [B] sites. The Zn^{2+} cations occupy preferentially tetrahedral sites, due to the covalent bonding effects [3]. The inversion degree defined as the fraction of Fe^{3+} cations in tetrahedral sites (A-sites) depends on synthesis condition. The highest inversion coefficient of 0.68 was achieved for φ=1 due to the sufficient distribution of cations originated from the higher combustion temperature.

The theoretical lattice parameter can be calculated by utilizing of the following equation [26]:

$$a_{th} = \frac{8}{3\sqrt{3}}\left[(r_A + R_O) + \sqrt{3}(r_B + R_O)\right] \quad \text{(eq. 10)}$$

which r_A and r_B are the radii of tetrahedral and octahedral sites and R_O is the radius of the oxygen ions (R_O=1.32 Å). The mean ionic radius of the tetrahedral (A) and octahedral [B] sites (r_A and r_B) can be calculated by the following relations [26]:

$$r_A = 0.2\, r_{Zn^{2+}} + (0.8-x)r_{Mn^{2+}} + x r_{Fe^{3+}} \quad \text{(eq. 11)}$$

$$r_B = \frac{1}{2}\left[x r_{Mn^{2+}} + (2-x)r_{Fe^{3+}}\right] \quad \text{(eq. 12)}$$

The theoretical (a_{th}) and experimental (a_{exp}) lattice parameters are given in Table 1. The agreement between a_{th} and a_{exp} indirectly verifies the cation distribution deduced from X-ray intensity calculations [28]. Table 1 also presents the crystallite size increases from 10 to 37 nm and then decreases to 25 nm with the increasing of fuel/oxidant molar ratio (ϕ) which is similar to the adiabatic combustion temperature.

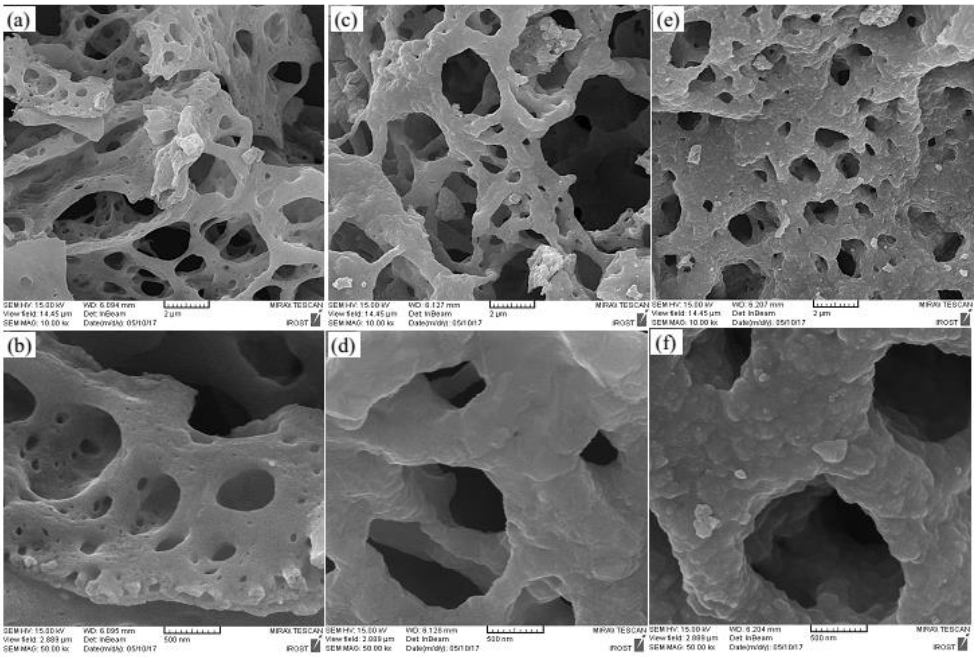

Fig. 2- SEM micrographs of the as-combusted $Mn_{0.8}Zn_{0.2}Fe_2O_4$ powders at (a and b) ϕ=0.5, (c and d) ϕ=1 and (e and f) ϕ=1.5.

SEM micrographs of the as-combusted $Mn_{0.8}Zn_{0.2}Fe_2O_4$ powders at the various ϕ values are compared in Fig. 2. The thermal energy and gases generated during the combustion reaction control the morphologies of as-combusted powders. The higher amounts of released gases increase the porosity and surface area, while the released thermal energy is the main factor for particle growth. The fuel type and fuel/oxidant ratio (ϕ) mainly effect on the released thermal energy and gases. The spongy structure and plenty of tiny pores are induced by escaping the large amount of gases. Although the amount of released gases increases with fuel content, but the amount and size of porosity decreases. It is reasonable to consider the released gas to fuel ratio, decreasing with fuel content [29]. The low combustion temperature at φ=0.5 leads to small particles with low crystallinity. The sintered particles in pore walls at φ=1 can be attributed to its highest adiabatic temperature. However, the rather large particles with high crystallinity at φ=1.5 are due to the complete combustion together with exhausting a large amount of gases.

Fig. 3 shows the magnetization curves of the as-combusted powders at the various fuel to oxidant ratios (φ). The values of saturation magnetization (Ms) and coercivity (Hc) as a function of fuel content are presented in Table 2. The saturation magnetization was calculated by plotting the high-field region of the M versus 1/H and extrapolating the data as $1/H \rightarrow 0$ (extrapolation to infinite field). The magnetic properties of spinel magnetic ferrite strongly depend on the phase, cation distribution, particle size and morphology and so on [6]. The saturation magnetization increases from 43 to 69 emu/g with the increase of φ from 0.5 to 1 and then slightly decreases to 67 emu/g for φ=1.5. The high purity and crystallinity of the as-combusted $Mn_{0.8}Zn_{0.2}Fe_2O_4$ powders at φ=1 result in the maximum saturation magnetization. With the increase of φ values from 0.5 to 1, the coercivity of the as-combusted powders increases from 27 to 60 Oe, due to the increase of crystallinity. However, the Hc slightly increases to 67 Oe for φ=1.5, due to its reduction of crystallite size. The increasing of domain walls as pinning factors for movement of

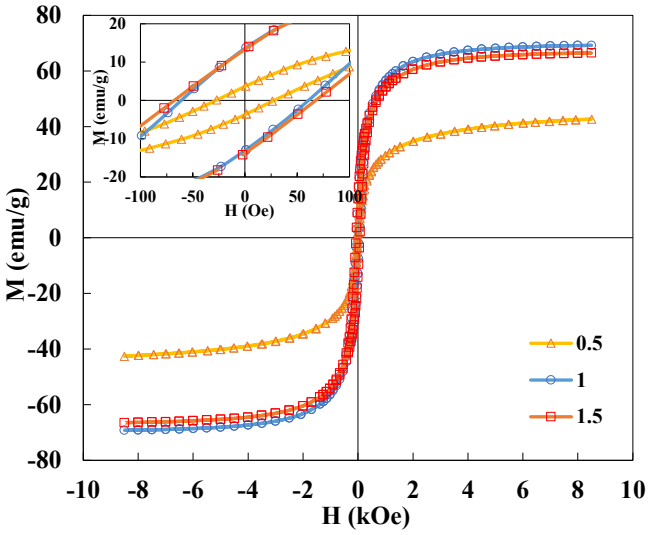

Fig. 3- Hysteresis loops of the as-combusted $Mn_{0.8}Zn_{0.2}Fe_2O_4$ powders.

Table 2- Magnetic properties of the as-combusted MnZn ferrite powders

Method	ϕ values	Ms (emu/g)	Hc (Oe)	Particle size (nm)	Reference
Solution combustion	0.5	43	27	10	This work
synthesis	1	69	60	37	
	1.5	66	67	25	
Coprecipitation		50		22	[20]
Hydrothermal		51		6	[28]
Thermal decomposition		15		22	[29]
Spark plasma sintering		83		1200	[9]
Ball milling		60		50	[30]

magnetic domains is responsible for the increase of coercivity with the decrease of crystallite size [30].

The saturation magnetization and crystallite size of the MnZn ferrite powders synthesized by the various physical and chemical methods are also listed in Table 2. The difference in the magnetic properties of the MnZn ferrite powders were mainly assigned to the difference in particle sizes. The larger particle size and higher crystallinity of solution combusted powders lead to the higher saturation magnetization [1, 9, 31-33].

4. Conclusions

Solution combustion synthesis has been used for preparation of single phase $Mn_{0.8}Zn_{0.2}Fe_2O_4$ powders. The $Mn_{0.8}Zn_{0.2}Fe_2O_4$ exhibited partially inverse structure in which Zn preferentially occupied tetrahedral (A) sites. The crystallite size increased from 10 to 37 nm and then decreased to 25 nm with the increase of fuel to oxidant ratio (φ values). The porosity of as-combusted powders decreased with fuel content. The highest saturation magnetization of 69 emu/g was achieved at φ=1 on account of the high purity and crystallinity.

References

1. Penchal Reddy M, Mohamed AMA, Venkata Ramana M, Zhou XB, Huang Q. Spark plasma sintering and microwave electromagnetic properties of MnFe2O4 ceramics. Journal of Magnetism and Magnetic Materials. 2015;395:185-9.
2. Duan L, Wang Y, Wang L, Zhang F, Wang L. Mesoporous MFe2O4 (M=Mn, Co, and Ni) for anode materials of lithium-ion batteries: Synthesis and electrochemical properties. Materials Research Bulletin. 2015;61:195-200.
3. Valenzuela R. Magnetic ceramics: Cambridge University Press; 1994.
4. Ghazanfar U, Siddiqi SA, Abbas G. Structural analysis of the Mn–Zn ferrites using XRD technique. Materials Science and Engineering: B. 2005;118(1-3):84-6.
5. Gajbhiye NS, Balaji G. Synthesis, reactivity, and cations inversion studies of nanocrystalline MnFe2O4 particles. Thermochimica Acta. 2002;385(1-2):143-51.
6. Goldman A. Modern ferrite technology. Springer Science & Business Media; 2006 Sep 28.
7. Masoudi MT, Saidi A, Hashim M, Hajalilou A. Comparison of structure and magnetic properties of Mn–Zn ferrite mechanochemically synthesized under argon and oxygen atmospheres. Canadian Journal of Physics. 2015;93(10):1168-73.
8. Akhtar MJ, Younas M. Structural and transport properties of nanocrystalline MnFe2O4 synthesized by co-precipitation method. Solid State Sciences. 2012;14(10):1536-42.
9. Meng YY, Liu ZW, Dai HC, Yu HY, Zeng DC, Shukla S, et al. Structure and magnetic properties of Mn(Zn)Fe2−xRExO4 ferrite nano-powders synthesized by co-precipitation and refluxing method. Powder Technology. 2012;229:270-5.
10. Li J, Yuan H, Li G, Liu Y, Leng J. Cation distribution dependence of magnetic properties of sol–gel prepared MnFe2O4 spinel ferrite nanoparticles. Journal of Magnetism and Magnetic Materials. 2010;322(21):3396-400.
11. Seyyed Ebrahimi SA, Masoudpanah SM, Amiri H, Yousefzadeh M. Magnetic properties of MnZn ferrite nanoparticles obtained by SHS and sol-gel autocombustion techniques. Ceramics International. 2014;40(5):6713-8.
12. Varma A, Mukasyan AS, Rogachev AS, Manukyan KV. Solution Combustion Synthesis of Nanoscale Materials. Chemical Reviews. 2016;116(23):14493-586.
13. Li F-t, Ran J, Jaroniec M, Qiao SZ. Solution combustion synthesis of metal oxide nanomaterials for energy storage and conversion. Nanoscale. 2015;7(42):17590-610.
14. Nersisyan HH, Lee JH, Ding J-R, Kim K-S, Manukyan KV, Mukasyan AS. Combustion synthesis of zero-, one-, two- and three-dimensional nanostructures: Current trends and future perspectives. Progress in Energy and Combustion Science. 2017;63:79-118.
15. Wen W, Wu J-M. Nanomaterials via solution combustion synthesis: a step nearer to controllability. RSC Adv. 2014;4(101):58090-100.
16. Seyyed Ebrahimi SA, Masoudpanah SM. Effects of pH and citric acid content on the structure and magnetic properties of MnZn ferrite nanoparticles synthesized by a sol–gel autocombustion method. Journal of Magnetism and Magnetic Materials. 2014;357:77-81.
17. Lazarova T, Georgieva M, Tzankov D, Voykova D, Aleksandrov L, Cherkezova-Zheleva Z, et al. Influence of the type of fuel used for the solution combustion synthesis on the structure, morphology and magnetic properties of nanosized NiFe 2 O 4. Journal of Alloys and Compounds. 2017;700:272-83.
18. Fathi H, Masoudpanah SM, Alamolhoda S, Parnianfar H. Effect of fuel type on the microstructure and magnetic properties of solution combusted Fe 3 O 4 powders. Ceramics International. 2017;43(10):7448-53.
19. Pourgolmohammad B, Masoudpanah SM, Aboutalebi MR. Effects of the fuel type and fuel content on the specific surface area and magnetic properties of solution combusted CoFe 2 O 4 nanoparticles. Ceramics International. 2017;43(11):8262-8.
20. Shafiu S, Topkaya R, Baykal A, Toprak MS. Facile synthesis of PVA–MnFe2O4 nanocomposite: Its magnetic investigation. Materials Research Bulletin. 2013;48(10):4066-71.
21. Yu H-F, Yang S-W. Formation of crystalline MnFe2O4 powder by flame-combusting freeze-dried citrate precursors. Journal of Alloys and Compounds. 2005;394(1-2):286-91.
22. Aruna ST, Mukasyan AS. Combustion synthesis and nanomaterials. Current Opinion in Solid State and Materials Science. 2008;12(3-4):44-50.
23. Mukasyan AS, Rogachev AS, Aruna ST. Combustion synthesis in nanostructured reactive systems. Advanced Powder Technology. 2015;26(3):954-76.
24. Skolnick LP, Kondo S, Lavine LR. An Improved X-Ray Method for Determining Cation Distribution in Ferrites. Journal of Applied Physics. 1958;29(2):198-203.
25. Cullity BD, Weymouth JW. Elements of X-Ray Diffraction. American Journal of Physics. 1957;25(6):394-5.
26. Sickafus KE, Wills JM, Grimes NW. Structure of Spinel. Journal of the American Ceramic Society. 2004;82(12):3279-92.
27. Najmoddin N, Beitollahi A, Kavas H, Majid Mohseni S, Rezaie H, Åkerman J, et al. XRD cation distribution and magnetic properties of mesoporous Zn-substituted CuFe2O4. Ceramics International. 2014;40(2):3619-25.
28. Zaki HM, Al-Heniti S, Al Shehri N. New scheme for cation distribution and electrical characterization of nanocrystalline aluminum doped magnesium ferrite MgAlxFe2−xO4. Physica B: Condensed Matter. 2014;436:157-63.
29. Pourgolmohammad B, Masoudpanah SM, Aboutalebi MR. Synthesis of CoFe 2 O 4 powders with high surface area by solution combustion method: Effect of fuel content and cobalt precursor. Ceramics International. 2017;43(4):3797-803.
30. Cullity BD, Graham CD. Introduction to Magnetic Materials: John Wiley & Sons, Inc.; 2008 2008/11/19.
31. Bateer B, Tian C, Qu Y, Du S, Yang Y, Ren Z, et al. Synthesis, size and magnetic properties of controllable MnFe2O4 nanoparticles with versatile surface functionalities. Dalton Transactions. 2014;43(26):9885.
32. Goodarz Naseri M, Saion EB, Ahangar HA, Hashim M, Shaari AH. Synthesis and characterization of manganese ferrite nanoparticles by thermal treatment method. Journal of Magnetism and Magnetic Materials. 2011;323(13):1745-9.
33. Zheng ZG, Zhong XC, Zhang YH, Yu HY, Zeng DC. Synthesis, structure and magnetic properties of nanocrystalline ZnxMn1−xFe2O4 prepared by ball milling. Journal of Alloys and Compounds. 2008;466(1-2):377-82.